JOURNAL OF APPLIED ELECTROCHEMISTRY **23** (1993) 933–942

Operational characteristics of laboratory scale alumina reduction cells with wettable cathodes

R. DORIN, E. J. FRAZER

CSIRO Institute of Minerals, Energy and Construction, Division of Mineral Products, P.O. Box 124, Port Melbourne, Victoria, 3207, Australia

Received 17 August 1992; revised 17 November 1992

The operational characteristics of a laboratory-scale alumina reduction cell incorporating a wettable cathode were evaluated by electrolyses in a 10 wt % alumina/cryolite melt at 975° C. It was shown that as the anode–cathode distance (a.c.d.) decreased, the mass transfer rate increased and the current efficiency decreased. The contribution to cell resistance from the anode bubble-layer at small a.c.d.'s was found to be significant. The ohmically corrected cell voltage decreased with decreasing a.c.d., increasing anode immersion and increasing anode rotation rate, indicating a substantial influence of mass-transfer on cell operation. Digital analysis of cell voltage and resistance data was used to characterize bubble behaviour over a range of operating conditions. The frequency spectra varied over the course of a run due to the cessation of the regular formation and detachment of large bubbles. Bubble behaviour was strongly dependent on anode geometry, current density and anode rotation rate, tending towards smaller bubbles at high angles of inclination, low current density and high rotation rate.

1. Introduction

The aluminium industry is currently developing wettable cathode technology based on titanium diboride/carbon composite materials. It is expected that such technology will allow a decrease in the interelectrode gap and a reduction in energy consumption [1]. Although there have been numerous laboratory and full-scale studies of traditional aluminium smelting cells, the amount of information available on the operation of cells with wettable cathodes and small anode–cathode distances (a.c.d.'s) is more limited. Karlsen *et al.* [2] compared the performance of solid wettable cathodes with liquid cathodes in a laboratory cell over a range of a.c.d. from 0.5 to 4.5 cm. Kasherman and Skyllas–Kazacos [3,4] have examined the effect of a.c.d on cell potential, and the effect of anode material and bath composition on the bubble-layer resistivity and the gaseous volume fraction, in cells with inclined electrodes. This paper reports on the operation of a newly developed laboratory cell, fitted with rotatable electrodes and a wettable cathode, allowing precise setting of a.c.d. and direct current efficiency measurement by full metal recovery.

Anode gas evolution has a significant influence on cell operation and it is anticipated that the detachment size, release frequency and layer thickness of bubbles will be some complex function of operating conditions, anode geometry, anode material, bath depth and bath composition. Investigations of anode gas evolution in aluminium smelting cells have mainly been restricted to modelling studies because of the difficulties involved in high temperature molten salt experimentation (see, for example, [5]). However, Utigard and Toguri [6] have observed anode gas behaviour during electrolysis at various current densities and melt compositions, using an X-ray radiographic technique. In the present study, digital signal analysis techniques have been employed to characterize bubble evolution behaviour over a range of operating conditions in a laboratory-scale cell.

2. Experimental details

2.1. *Electrochemical cell*

A multi-element graphite electrochemical cell was designed with the object of conserving as much of the body as possible from run to run (see Fig. 1). A molybdenum cathode was employed which enabled the formation of a stable aluminium film and allowed virtually complete recovery of the aluminium product for analysis. The sides of the cathode were tapered to allow sealing into a tapered boron nitride (Union Carbide, HBR grade) insulating ring. A stainless steel retaining screw, inserted from the bottom of the outer graphite (Morganite EY941) sheath, clamped the tapered cathode assembly, and inner and outer graphite sheaths firmly together. The use of an outer graphite sheath allowed complete removal of the cell assembly from the graphite support shell. The inner graphite (EY911) sheath, which facilitated melt removal, was electrically isolated from the cathode by a boron nitride support. An argon atmosphere was maintained within the Inconel furnace tube to prevent excessive oxidation of the graphite cell components.

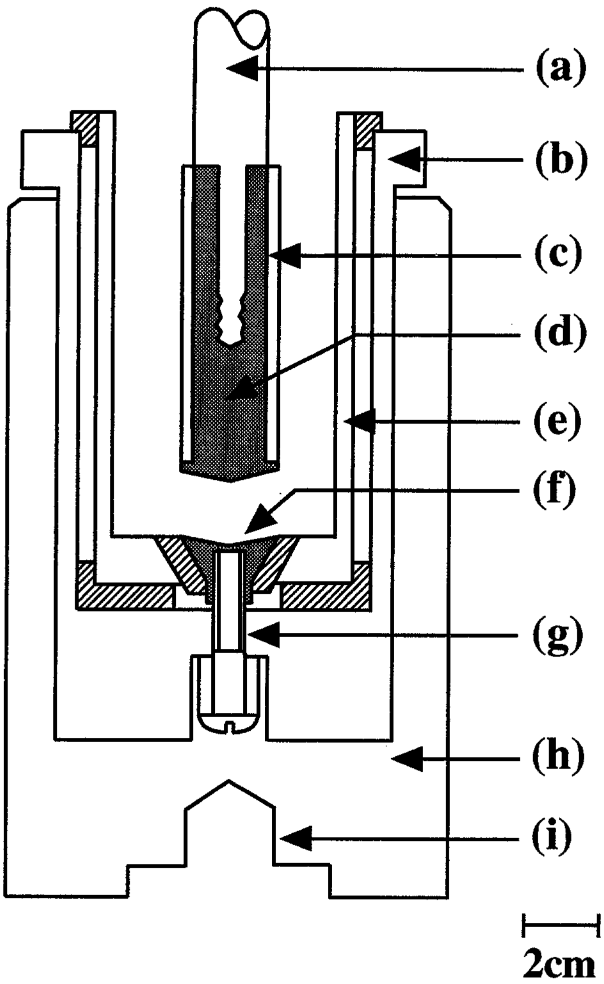

Fig. 1. Schematic of multi-element graphite experimental cell; (a) Inconel rotator shaft, (b) outer graphite sheath, (c) recrystallized alumina sheath, (d) graphite anode, (e) inner graphite sheath, (f) molybdenum cathode, (g) retaining screw, (h) graphite support shell, (i) rotator mount; (hatched areas = boron nitride).

Anodes were fabricated from EY941 graphite rod and sheathed with recrystallized alumina tubing (Alsint, 99.7%) to define the active surface area. The majority of the work was performed using a horizontal 24 mm diameter anode, with an unsheathed 1.5 mm thick section to allow for consumption during electrolysis. The working face of the anode was of conical cross-section, usually with a 5° inclination. The molybdenum cathode was 25 mm in diameter and had a complementary conical cross-section to the anode.

The cell was contained in an Inconel 600 furnace tube which was designed to allow crucible rotation via an Inconel shaft entering the tube from below through a high temperature bearing. An electrode rotator (Pine Instrument Company Model AFASRE) was mounted above the furnace and fitted with an extended Inconel arbour which entered the cell through a water cooled bearing in the lid. These features were planned to give better control over mass transfer, although the simulation of the hydrodynamics of industrial cells can only be approached at a much larger scale than the present laboratory cell. The unit was heated by an 8 kW Globar (The Carborundum Co.) furnace with appropriate power and temperature control units.

2.2. *Melt composition*

Alumina and synthetic cryolite, supplied by Comalco Research Centre (CRC), were vacuum dried at approximately 120° C for 4 h and then stored under vacuum until required. A 10 wt % alumina/cryolite melt composition was used at 975° C for all experimental work. This high alumina concentration allowed the operation of the cell for reasonable periods without significant depletion of the alumina and also minimized attack on the Alsint anode sheath; during a normal run of $\sim$ 80 min at 5 A, the alumina concentration would be reduced by 10–12%. The copper oxide used in mass transport determinations was BDH Analar reagent grade.

2.3. *Electrochemical measurements*

Electrodeposition current was supplied by a 5 A capacity constant-current unit and the charge passed during electrolysis was metered by a coulometer. Both these units were designed and constructed in these laboratories [7]. The cell impedance was evaluated by modulating the applied current at 1 kHz and comparing the amplitude ratio and phase difference of the 1 kHz components of the cell voltage and cell current. The phase difference was always small ($<2°$) indicating that the real (i.e. resistive) part of the impedance was very close to the measured value. Therefore, the latter value was taken as being equal to the cell resistance. The cell voltage and resistance were continuously monitored on a Rikadenki multipen *Y–t* chart recorder and the average values were used to prepare plots as required. The cell voltage and resistance measurements were periodically sampled using a Keithley 'Metrabyte' DAS-HRES 16 bit multi-channel A/D interface board in an IBM-PC/XT compatible computer driven by software routines written in QuickBASIC (Microsoft Corp.). The digitally collected data were analysed using DADiSP 3.0 (DSP Development Corp.) data analysis and display software. In the analysis of the data it was assumed that the anode gas evolution was the major cause of the fluctuations in cell voltage, as has been demonstrated by Singh *et al.* [8] for the electrowinning of manganese from molten chlorides.

2.4. *Mass transfer measurements*

A range of metal ions was considered to determine their suitability as tracer ions for mass transfer measurements. Current–voltage curves were recorded in a 10 wt % alumina/cryolite melt containing $\sim$ 0.1 wt % CuO at 975° C on a rotating gold-coated molybdenum working electrode. It was found that the limiting current for copper deposition was linear with the square root of cathode rotation rate, indicating that this reduction is diffusion controlled in cryolitic melts. Using published data for melt viscosity and density [9], a diffusion coefficient of $7.3 \times 10^{-5}\,\mathrm{cm^2\,s^{-1}}$ for copper was calculated. Having established the suitability of copper as a tracer ion for mass transfer measurements, it was generally added to melts as CuO in trace amounts (0.01 wt %). The aluminium product was analysed for codeposited copper by atomic absorption spectroscopy (AAS) and the data used in the determination of mass transfer rates

3. Results and discussion

3.1. *Electrochemical characteristics*

3.1.1. Effect of a.c.d. *on current efficiency.* Current efficiencies (c.e.) were determined without electrode rotation over a range of a.c.d. from 0.25 to 5.0 cm. Electrolyses were run at a current density of $1\,\mathrm{A\,cm^{-2}}$ for 80 min (i.e. 24 000 C) and the melt then quickly frozen to prevent product losses. After cooling and disassembly of the cell, the aluminium disc was recovered from the cathode, cleaned and weighed. The c.e. was then calculated using the theoretical weight of aluminium derived from Faraday's law. The reproducibility of these determinations was very dependent upon a.c.d. with a spread (in c.e.) of 0.5% at 3 cm to about 6% at 0.25 cm.

The effect of a.c.d. on current efficiency is shown in Fig. 2. The graph suggests the existence of a maximum efficiency of ~ 85% at an a.c.d. of ~ 3 cm. The c.e. gradually decreased with decreasing a.c.d. down to about 1.5 cm, beyond which it rapidly decreased, falling to around 62% at 0.25 cm, probably as a result of increased interaction between the aluminium product and the anode gas. These observations are in good agreement with those of Karlsen *et al.* [2].

3.1.2. Effect of a.c.d. on mass transfer rate. Electrolyses were run over an a.c.d. range of 0.25 to 5 cm at $1\,\mathrm{A\,cm^{-2}}$ as above. The aluminium disc was recovered as before and analysed for copper content by AAS. Although the data are very scattered, the plot of mass of copper codeposited with aluminium against a.c.d. (see Fig. 3) suggests that, at a.c.d.'s less than ~ 0.75 cm, the mass transfer rate to the cathode is being enhanced. Such an effect could be due to increased melt velocities induced by the evolution and flow of anode gas bubbles in more restricted gaps. At larger a.c.d.'s, the mass transfer rate does not appear to vary in any systematic manner.

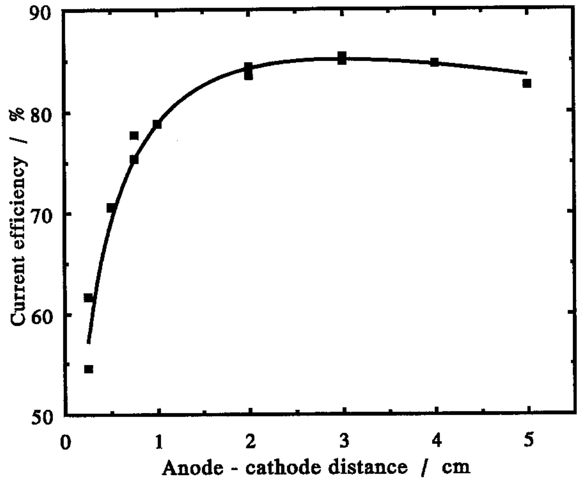

Fig. 2. The effect of a.c.d. on current efficiency of alumina reduction in a 10 wt % alumina/cryolite melt at 975° C ($1\,\mathrm{A\,cm^{-2}}$; 24 000 C).

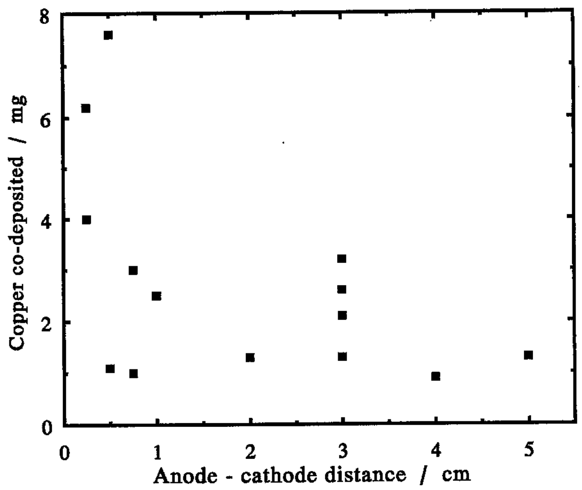

Fig. 3. Plot of copper codeposited with aluminium against a.c.d. in a 10 wt % alumina/cryolite melt at 975° C ($1\,\mathrm{A\,cm^{-2}}$; 24 000 C).

Using the average value for the copper deposited at each a.c.d. (data from Fig. 3), the limiting current for copper deposition and hence the mass transfer coefficient for copper (k_{Cu}) were calculated, viz:

$$k_{\mathrm{Cu}} = i_{\mathrm{L}}/nFC_{\mathrm{b}} \tag{1}$$

where i_{L} is the limiting current density for copper deposition, C_{b} is the bulk copper concentration (log-mean average) in the melt, n is the number of electrons transferred and F is the Faraday constant. Assuming laminar flow, the mass transfer coefficient for aluminium (k_{Al}) was then calculated using the following relationship [10]:

$$k_{\mathrm{Al}} = k_{\mathrm{Cu}}\left(\frac{D_{\mathrm{Al}}}{D_{\mathrm{Cu}}}\right)^{0.75} \tag{2}$$

and plotted against a.c.d. in Fig. 4. A diffusion coefficient of $5.4 \times 10^{-5}\,\mathrm{cm^2\,s^{-1}}$ for aluminium (D_{Al}) in a melt with similar cryolite ratio ($CR = 3$) [11] and the calculated diffusion coefficient for copper (D_{Cu}) (Section 2.4) were used in the above equation for the determination of k_{Al}. As before, a significant increase in the mass transfer rate can be seen at a.c.d.'s less than ~ 0.75 cm.

It is interesting to note that a plot of c.e. against mass transfer rate, using the data from Figs 3 and 4, is essentially linear (Fig. 5). Assuming that the rate of reaction between 'dissolved' aluminium and the anode gas bubbles is fast, and that the solubility of the metal is much higher than the anode gas, the above relationship suggests that the loss in c.e. is controlled by the diffusion of aluminium from the cathode surface. Such a mechanism is essentially in agreement with a commonly accepted view of current

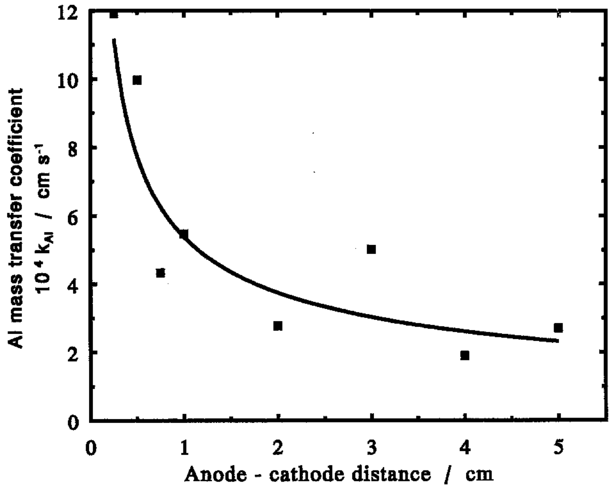

Fig. 4. Plot of mass transfer coefficient for aluminium against a.c.d. in a 10 wt % alumina/cryolite melt at 975° C (1 A cm^{-2}; 24 000 C).

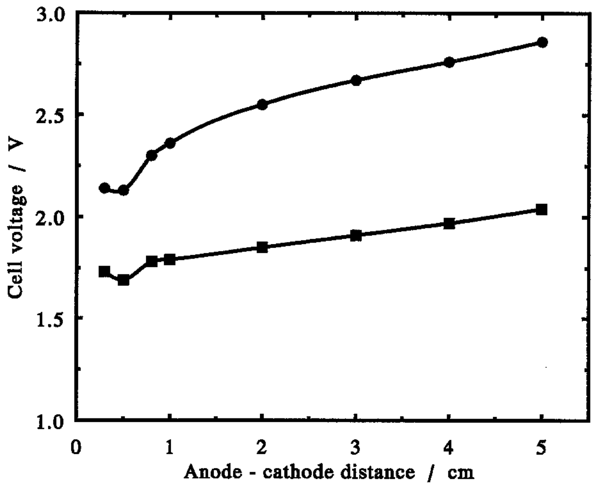

Fig. 6. Plot of cell voltage against a.c.d. in a 10 wt % alumina/cryolite melt at 975° C (1 A cm^{-2}); (●) uncorrected; (■) corrected for *IR*.

efficiency loss, *viz*, by reaction between gaseous CO_2 and dissolved metal [12].

3.1.3. Effect of a.c.d. on cell voltage. A plot of cell voltage against a.c.d. recorded during a single run is shown in Fig. 6. The figure shows both the actual cell voltage and the voltage corrected for ohmic voltage drop (*IR*). The dip in cell voltage at an a.c.d. of 0.5 cm is reproducible and may be related to bubble-layer thickness or cell geometry, but no further explanation can be suggested. The corrected cell voltage increases with increasing a.c.d. (300 mV over 5 cm) suggesting a significant mass transfer influence. There may also be an additional effect on the cell voltage resulting from the change in current distribution due to the unshielded edge of the anode. Because these data were obtained by varying the a.c.d., without changing the melt volume, the results also reflect the change in depth of anode immersion (a.i.) with change in a.c.d.; this latter effect is discussed in the following section.

3.1.4. Effect of a.i. on cell voltage. A series of experiments was conducted to evaluate the effect of a.i. on cell voltage at constant a.c.d. The melt volume was adjusted to give the required a.i. at an a.c.d. of 2 cm. A plot of cell voltage against a.i. is shown in Fig. 7. The observed decrease in cell voltage with increasing anode immersion cannot be due to any increase in anode surface area because the electrode is shielded preventing significant variation in current density and current distribution. The decrease appears, therefore, to be due to a mass transfer effect related to that found for a.c.d.

The relationship between corrected cell voltage and a.i. can be approximated by the following expression:

$$(V - IR) = 1.95 - 0.03 \times (\text{a.i.}) \qquad (3)$$

where $(V - IR)$ is in volts and a.i. in cm. Using this relationship, the plot of cell voltage against a.c.d. (Fig. 6) was corrected for the different a.i. at each respective a.c.d., using the result at 2 cm as the reference position. The resultant plot (Fig. 8) shows that the variation in a.i. accounts for more than 50% of the change in cell voltage with a.c.d. This confirms that a.c.d. has some independent effect on cell voltage which has been attributed to a mass transfer effect (Section 3.1.3.), without which, one would expect the corrected plot to be a horizontal line.

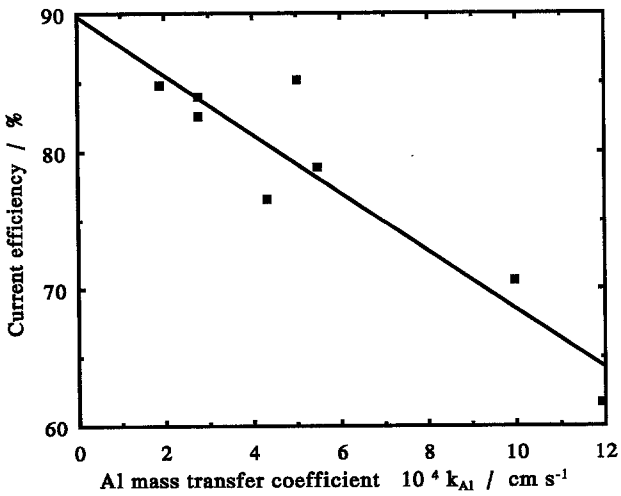

Fig. 5. Plot of c.e. against mass transfer coefficient for aluminium in a 10 wt % alumina/cryolite melt at 975° C (1 A cm^{-2}; 24 000 C).

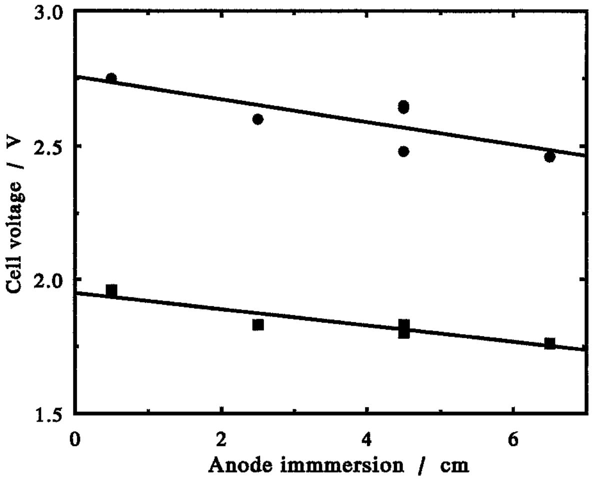

Fig. 7. Effect of anode immersion on cell voltage at a constant a.c.d. of 2 cm in a 10 wt % alumina/cryolite melt at 975° C (1 A cm^{-2}); (●) uncorrected; (■) corrected for *IR*.

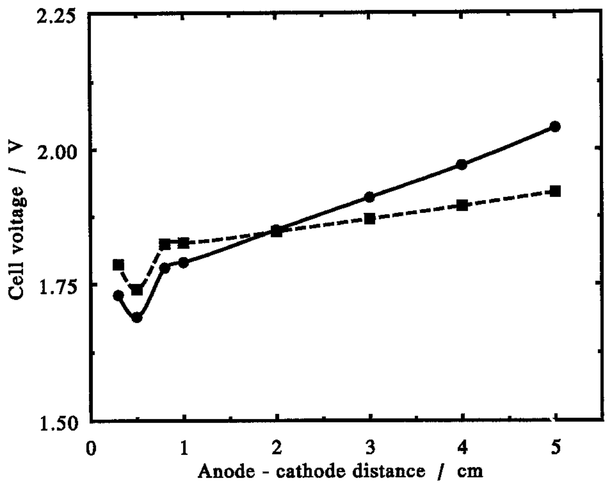

Fig. 8. Variation in cell voltage, corrected for *IR* and a.i., with a.c.d. in a 10 wt % alumina/cryolite melt at 975° C (1 A cm^{-2}); (●) corrected for *IR*; (■) corrected for *IR* and a.i.

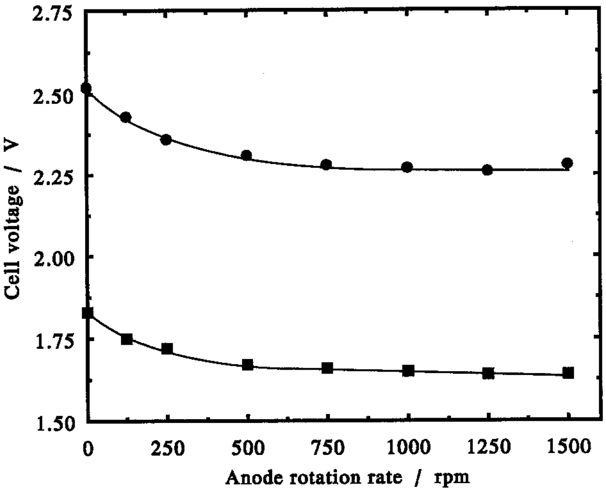

Fig. 10. Effect of anode rotation rate on cell voltage in a 10 wt % alumina/cryolite melt at 975° C (a.c.d. = 2 cm); (●) uncorrected; (■) corrected for *IR*.

3.1.5. Effect of a.c.d. on excess cell resistance. The cell resistance recorded during each run represented the total resistance between the two probe points, i.e. it included all contact, conductor and melt contributions. An estimate of the combined contact and conductor resistance during electrolysis was obtained by momentarily shorting the anode to the cathode; a value of 0.031 Ω was obtained. The resistance recorded at the various a.c.d.'s was then adjusted using this figure. The difference between the adjusted value and the melt resistance, calculated from published data [13] and assuming that the current path is restricted to the cylindrical channel joining the anode and cathode, was plotted against a.c.d. (Fig. 9).

The plot shows that for a.c.d.'s above ~ 1.3 cm, the effective resistance is less than that expected from the calculated melt resistance. This reflects the increased cross-sectional area available for current flow as a consequence of the relatively large ratio of cell diameter to electrode diameter, the effective cross-sectional area increasing as a.c.d. is increased. At lower a.c.d.'s, the increased value of the cell resistance is presumably due to the contribution from the bubble layer. An excess resistance value of 0.046 Ω at 5 A and 0.5 cm a.c.d. is equivalent to an increase in cell voltage of 230 mV, which is ~ 10% of the observed cell voltage! The crossover point in Fig. 9, at around 1.3 cm, can be interpreted as the point where the increase in cell resistance due to the bubble layer is counterbalanced by the decreasing cell resistance caused by the increase in effective cross-sectional area. From a number of experiments the crossover point was found to vary over the range 0.9 to 1.3 cm.

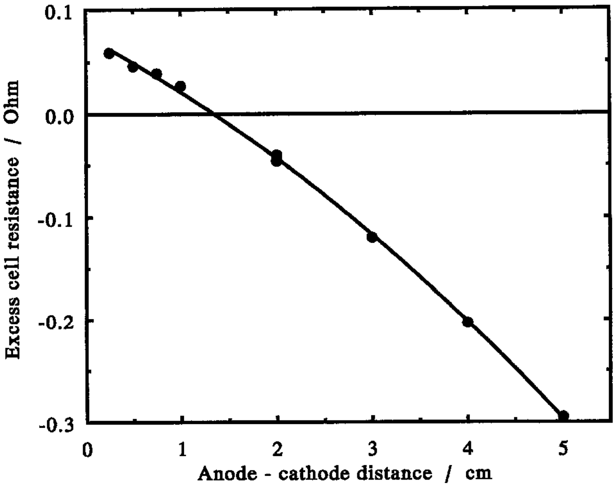

Fig. 9. Plot of calculated excess cell resistance against a.c.d. in a 10 wt % alumina/cryolite melt at 975° C (1 A cm^{-2}).

3.1.6. Effect of anode rotation rate on cell voltage. Figure 10 shows the variation of cell voltage with anode rotation rate over the range 0 to 1500 r.p.m., at an a.c.d. of 2 cm. At rotation rates up to ~ 600 r.p.m., the corrected cell voltage gradually decreased from 1.83 to 1.66 V; from 750 to 1500 r.p.m. it varied by only 20 mV. Depending on the degree of anodic concentration polarization at the current density of 1 A cm^{-2}, this behaviour could also suggest a change in surface coverage, i.e. a change in the rate of bubble-growth, coalescence and detachment, and/or bubble size. Leistra and Sides [14] reported decreases in potential of smaller magnitude than observed here, but on cylindrical electrodes where bubble evolution should be less restricted.

3.1.7. Effect of cathode rotation rate on cell voltage. Figure 11 shows the variation of cell voltage with cathode rotation rate over the range 0 to 50 r.p.m. at an a.c.d. of 2 cm. As can be seen, there is no effect apparent on the cell voltage over this range implying that convective stirring is dominant under these conditions.

3.1.8. Effect of anode geometry on cell voltage. An indication of the effect of the anode geometry on cell voltage was obtained from electrolyses using conical anodes with 0, 5 and 48° inclinations, at an average a.c.d. of 2 cm. Given the relatively large a.c.d., it was considered unnecessary to vary the cathode

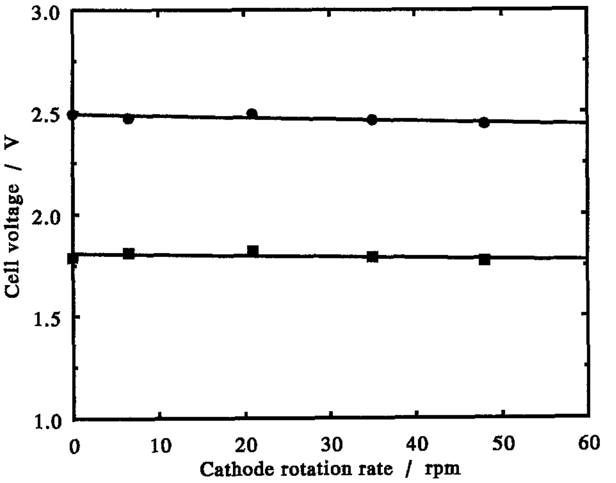

Fig. 11. Effect of cathode rotation rate on cell voltage in a 10 wt % alumina/cryolite melt at 975° C (a.c.d. = 2 cm); (●) uncorrected; (■) corrected for *IR*.

angle (5°) for these runs. The amplitude of the *fluctuations* in cell voltage (see, for example, W1 of Fig. 14), which would be expected to be independent of the change in current distribution with anode inclination, increased from around 80 mV at 48° to ~ 150 mV at 5° to 100–300 mV at 0°. Assuming that the cathode potential remains essentially constant, this behaviour presumably reflects the tendency for the release of smaller bubbles from the anode as the inclination is increased; there may also be an accompanying change in the degree of surface coverage by the anode gas.

3.1.9. Cell current–voltage relationship. The current–voltage relationship for the laboratory cell was plotted over the range 0.1 to 1 A cm^{-2} and is shown in Figure 12. There appears to be a change in slope at a current density of ~ 0.6 A cm^{-2}, which corresponds to a corrected cell voltage of ~ 1.85 V. Assuming that the response is principally due to the anode reaction, this behaviour suggests either a shift in mechanism for gas evolution or a change in surface coverage.

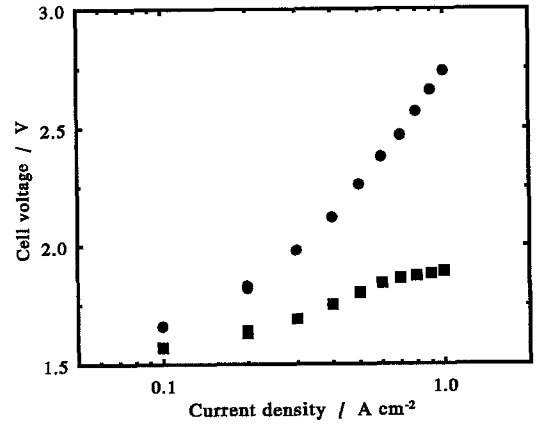

Fig. 12. Current-voltage relationship in a 10 wt % alumina/cryolite melt at 975° C (a.c.d. = 2 cm); (●) uncorrected; (■) corrected for *IR*.

3.2. *Anode gas bubble phenomena*

3.2.1. Time dependence at constant a.c.d. Cell voltage and cell resistance data were digitally sampled (usually at 100 Hz over 40 s intervals) at various times during a run under a standard set of experimental conditions (1 A cm^{-2}, 80 min, a.c.d. 2 cm, a.i. 4.5 cm) and processed using the DADiSP software. A typical analysis at $t = \sim 7$ min is shown in Fig. 13. Window W1 shows the data as a voltage/time display, and window W2 displays an extract of the voltage frequency spectrum from 0 to 5 Hz. The dominant frequency in W2 is 0.3 Hz which can be interpreted, by referring back to W1, as a bubble detachment frequency.

The increase in cell voltage *between* bubble detachments has been analysed separately. The fine structure revealed in W3 can be interpreted as the formation of large bubbles via a sequence of smaller bubble-growth/coalescence events, which precede their detachment. The spectrum of this voltage behaviour (W4) shows a spread of frequencies from 0 to 7 Hz (at amplitudes above the background noise level), with the larger voltage fluctuations in the 0 to 2 Hz range.

The spectrum of the cell voltage was found to change over the course of the experiment. In the early stages, the presence of a dominant detachment frequency varying from 0.25 to 0.4 Hz masked the background spectrum of bubble generation/coalescence in the 0 to 7 Hz range. Figure 14 shows the frequency spectrum near the end of the run where the regular buildup and detachment of large bubbles no longer occurred. In this case, the dominant frequency degenerated into a spread of frequencies appearing as a broad 'hump' on the background spectrum of bubble evolution which was not particularly reproducible from run to run. Overall, this behaviour suggests the development of a gas-evolving surface during the course of the run, which favours the evolution of smaller bubbles. For this reason, all comparative evaluations discussed in the following sections were made after stable conditions had been established (usually at $t > 20$ min).

3.2.2. Calculation of mean bubble radius. Gabrielli *et al.* [15] have developed a method for the estimation of mean bubble radius $\langle r_d \rangle$ from the power spectral density of the potential fluctuations during gas evolution under galvanostatic control, using the expression:

$$\langle r_d \rangle = \frac{r_e \langle \Delta\eta^2 \rangle^{1/4}}{(R_e I \alpha_e)^{1/2}} \tag{4}$$

where r_e is the radius of the disc electrode in centimetres, $\langle \Delta\eta^2 \rangle$ is the mean value of the square of the total overpotential jump amplitude due to a bubble departure (V^2), R_e is the electrolyte resistance (Ω), I is the electrolysis current (A) and α_e is a dimensionless proportionality constant which reflects the degree of shading of the current on the electrode sur-

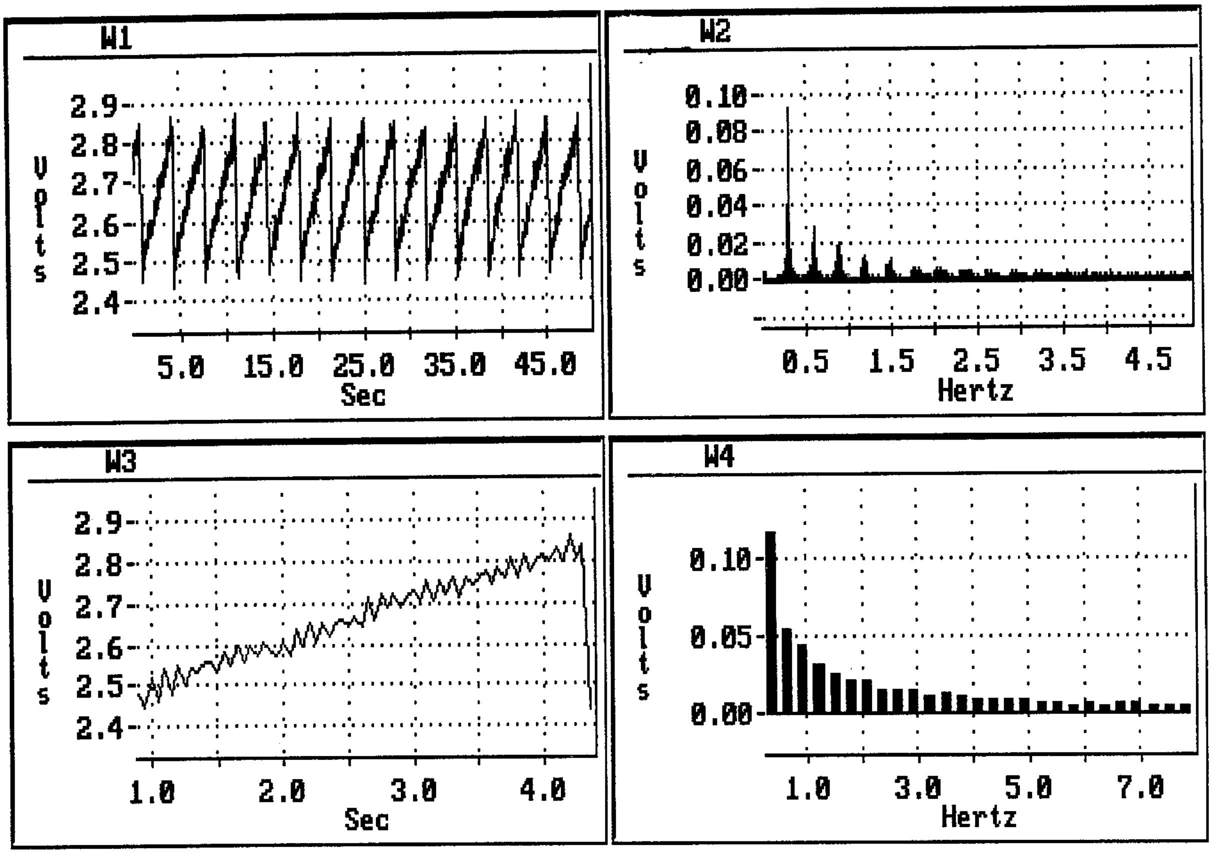

Fig. 13. Typical digital analysis by DADiSP software of voltage data for an electrolysis under standard conditions (a.c.d. = 2 cm; t = 7 min); W1: cell voltage; W2: frequency spectrum of W1; W3: single rising portion of W1; W4: frequency spectrum of W3.

face by the presence of non-conducting bubbles. The above equation implies that, for a constant retained gas volume, the contribution by the bubble layer to cell resistance decreases as the bubble size increases. Recently, Hyde and Welch [16] have provided experimental confirmation of this trend in a molten salt system, using ceramic spheres to simulate the presence of bubbles during the electrolysis process.

Gabrielli *et al.* also showed [15, 17] that the constant α_e could be determined independently by measurement of the change in cell resistance which occurs following the detachment of an insulating sphere simulating a bubble, viz:

$$\alpha_e = \frac{\Delta R_e r_e^2}{R_e r_b^2} \tag{5}$$

where r_b is the radius of the insulating sphere, R_e is the electrolyte resistance in the *absence* of the sphere and ΔR_e is the change in electrolyte resistance due to the departure of the sphere.

To enable the determination of α_e using the above equation, a sphere of BN was attached via a thin BN spigot to the centre of an anode to simulate the presence of a single non-conducting bubble. Resistance measurements were taken at various a.c.d.'s before separating the sphere from the anode by forcing it against the molybdenum cathode while rotating the cell. Being less dense than the melt, the BN sphere floated to the surface where it no longer interfered with the current distribution between the electrodes. The resistance measurements were then repeated in the absence of the sphere.

The estimation of α_e was found to be affected by the simultaneous gas evolution occurring at normal

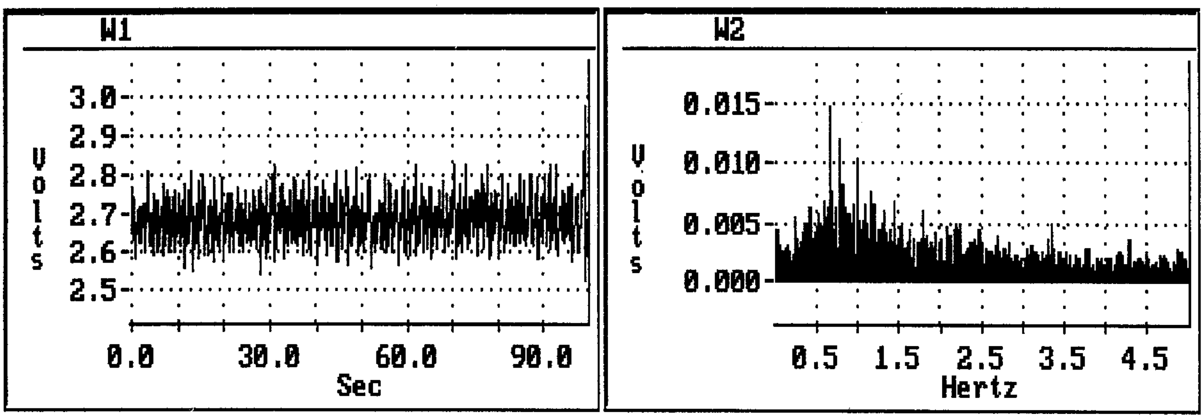

Fig. 14. Cell voltage (W1) and frequency spectrum (W2) for an electrolysis under standard conditions (a.c.d. = 2 cm; t = 70 min.).

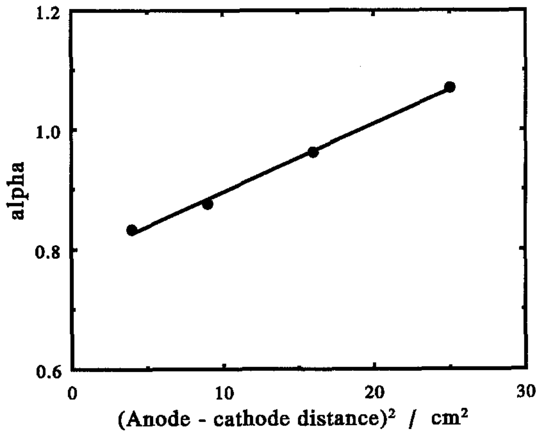

Fig. 15. Plot of α_e against (a.c.d.)^2 in a 10 wt % alumina/cryolite melt at 975° C (8 mm dia. BN sphere; 0.1 A cm^{-2}).

operating current densities (1 A cm^{-2}), masking the change in cell resistance. This effect was most pronounced with a BN ball of $\sim$ 8 mm diameter suggesting a similar bubble layer thickness, consistent with literature reports [18]. Hence, the resistance measurements were made at a reduced current density of 0.1 A cm^{-2}, where bubble formation was greatly reduced. The constant α_e was found to vary linearly with (a.c.d.)^2 (Fig. 15), presumably as a result of the particular geometry and current distribution in the laboratory cell. The value of α_e at any given a.c.d. (cm) could be determined from the expression:

$$\alpha_e = 0.0115 \times (\text{a.c.d.})^2 + 0.78 \qquad (6)$$

A mean bubble radius of 0.46 mm was calculated using Equations 6 and 4 for a typical run under the following conditions: a.c.d. 2 cm ($\alpha_e = 0.83$), anode radius 1.2 cm, $I = 4.985$ A, $R_e = 0.107\,\Omega$ and the experimentally determined value of $\langle \Delta\eta^2 \rangle = 4.36 \times 10^{-7}$ V^2.

3.2.3. Effect of a.i. at constant a.c.d. A series of experiments was conducted under standard conditions at anode immersions of 0.5, 2.5, 4.5 and 6.5 cm with the a.c.d. held constant at 2 cm. The cell voltage and resistance data were collected and analysed as before (Section 3.2.1). The spectra recorded at each immersion depth and the calculated $\langle r_d \rangle$ did not significantly vary. Although one might anticipate some dependence of bubble behaviour on a.i., the apparent independence could be related to the chosen a.c.d. and particular cell geometry, viz the low ratio of anode diameter to cell diameter. However, as a.i. increases, the melt stirring, induced by the bubbles rising through an increased path length, would be expected to increase. This is consistent with the observed decrease in cell voltage and the mass transfer effect suggested in Section 3.1.4.

3.2.4. Effect of a.c.d. A further series of experiments was conducted over a range of a.c.d. while using a constant melt volume, thus allowing the a.i. to increase with decreasing a.c.d. Spectral analyses of these experiments revealed no trend in bubble frequency with a.c.d. over the range 0.5 to 5 cm. However, the $\langle r_d \rangle$ increased by a factor of $\sim$ 2 in going from 5 to 0.25 cm, with an accelerated increase at a.c.d.'s < 1 cm. This behaviour suggests that the effect of anode immersion becomes significant at small a.c.d.'s in contrast to that observed at 2 cm (Section 3.2.3).

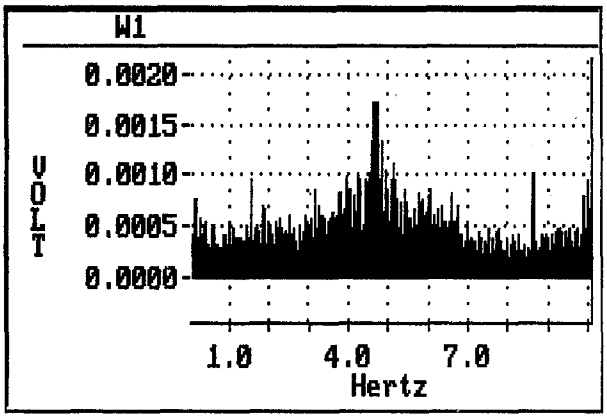

Fig. 16. Frequency spectrum of cell voltage at a.c.d. of 0.25 cm ($t = 78$ min).

At an a.c.d. of 0.25 cm the spectra gradually spread from the 0 to 4 Hz to the 0 to 7 Hz range over the course of the run, with the 'hump' moving from 1 to 4 Hz; at no time was there evidence of a dominant detachment frequency. Figure 16 depicts the spectrum at $t = 78$ min and Fig. 17 shows the change in bubble frequency over the course of the run. The calculated mean bubble radius ($\langle r_d \rangle$) decreased rapidly at first and then more gradually over the remainder of the run (from 0.94 to 0.38 mm). Also, there was a strong inverse correlation between the frequency of the 'hump' and $\langle r_d \rangle$.

3.2.5. Effect of anode geometry. It has already been shown that the anode geometry affects the amplitude of the cell voltage fluctuations (Section 3.1.8). The spectra of the cell voltages for anodes with 0, 5 and 48° inclinations (at an average a.c.d. of 2 cm) were recorded and compared at $t = 20$min. While the frequency spectra did not vary significantly, the calculated $\langle r_d \rangle$ decreased from 0.75 to 0.45 to 0.24 at 0, 5 and 48° respectively, implying

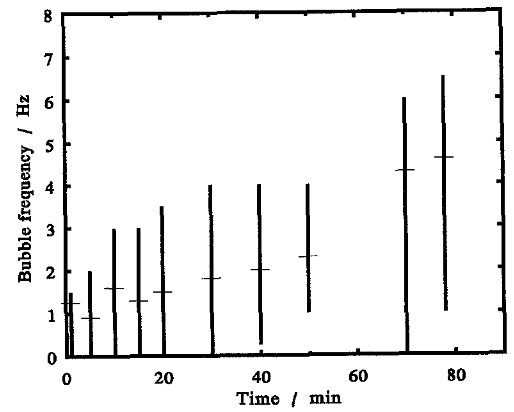

Fig. 17. Plot of bubble frequency against electrolysis time at an a.c.d. of 0.25 cm. Bars show spread of frequency and markers show position of 'hump' at each time.

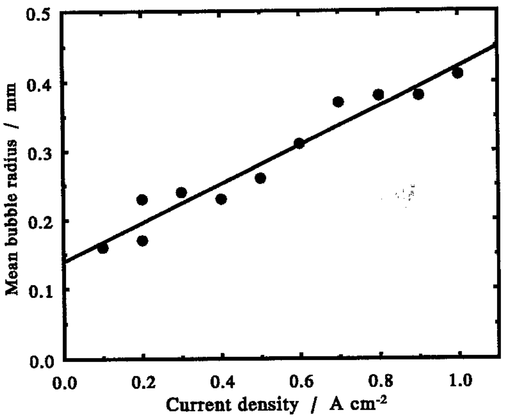

Fig. 18. Plot of calculated mean bubble radius against current density (a.c.d. = 2 cm).

a reduction in bubble coalescence rate as the anode inclination is increased; there may also be a corresponding reduction in the bubble layer thickness.

3.2.6. Effect of anode and cathode rotation rates. Measurements were taken of the spectra of cell voltages at anode rotation rates in the range 0 to 1500 r.p.m. after cell operation had stabilized. Although the frequency distribution of the cell voltage spectra did not vary significantly over this range, the $\langle r_d \rangle$ decreased from 0.47 to 0.23 mm in going from 0 to 500 r.p.m. Above this rotation rate, the mean bubble radius did not vary significantly. This overall behaviour is consistent with the interpretation put forward in Section 3.1.6.

Measurements were also taken over a small range of cathode rotation rate (0–50 r.p.m.). The calculated $\langle r_d \rangle$ increased by a factor of ~ 2, from 0.47 to 0.99 mm, over the range studied. This behaviour may be due to the influence on the anode-gas bubbles of the centripetal force generated by the induced rotation of the melt, restraining bubble departure and forcing an increase in holdup, coalescence rate, and hence, average bubble size. The invariance of cell voltage found over the same cathode rotation range (Fig. 11) can be reconciled with the above observations, since any increase in cell resistance due to increased gas holdup would tend to be compensated by the decrease in resistance as bubble size increases (Section 3.2.2).

3.2.7. Effect of current density. Measurements were taken over a range of current density varying from 0.2 to 1 $\mathrm{A\,cm^{-2}}$. A relative increase in the overall amplitude of the voltage fluctuations was observed which can be explained in terms of the increased rate of gas generation. A plot of the calculated mean bubble radius as a function of current density (shown in Fig. 18) is linear and can be compared with a one-third power dependence found by Gabrielli *et al.* [15] for evolution of oxygen and hydrogen in aqueous solutions. The ratio of the $\langle r_d \rangle^3$ at 1.0 $\mathrm{A\,cm^{-2}}$ to that at 0.2 $\mathrm{A\,cm^{-2}}$ is approximately ten, which is twice that expected if the same number of bubbles were being formed. Thus the change in $\langle r_d \rangle$ with current density suggests an increase in the rate of coalescence as the current density is increased.

4. Conclusions

Overall, the a.c.d. was found to be the most important factor in determining the current efficiency, cell voltage and cell resistance. The current efficiency reached a maximum of $\sim 85\%$ at an a.c.d. of ~ 3 cm and decreased rapidly at spacings less than 1.5 cm. The behaviour was considered to be indicative of an increasing interaction between the anode gas and the aluminium product, as the a.c.d. was decreased.

From the copper tracer-ion experiments, the mass transfer coefficient for the aluminium species was found to increase significantly at small a.c.d.'s (< 0.75 cm). Using the common independent variable, a.c.d., it was possible to show that a linear relationship existed between the current efficiency and the mass transfer rate. This correlation is a further confirmation of the importance of mass transfer in cell operation and design. Also, both a.c.d. and a.i. affected true cell voltage, presumably as a result of their influence on the mass transfer characteristics of the cell.

The characteristic behaviour of bubble evolution, as could be inferred from the spectra of cell voltage and resistance measurements, varied with electrolysis time. Under some conditions, a dominant bubble detachment frequency could be observed in the early stages of an electrolysis. This was superimposed on the normally observed spectra of bubble-related events which occurred over the 0 to 7 Hz range. The apparent reduction in the formation of large bubbles, which occurred after the initial stages of electrolysis (usually ~ 20 min), could be due to the development of the anode surface and/or changes in interfacial properties brought about by the buildup of dissolved metal in the melt [19]. It is unlikely that the small reduction in alumina concentration within this time ($\sim 3\%$) would significantly alter the physical properties of the melt.

Bubble evolution behaviour seemed to be independent of a.i. at an a.c.d. of 2 cm. However, the mean bubble radius increased by a factor of ~ 2 over the a.c.d. range 5 to 0.25 cm, with an accelerated increase at less than 1 cm. The corresponding change in cell resistance over the same a.c.d. range, revealed a significant contribution by the anode bubble layer to the resistance at small a.c.d.'s (< 1 cm). Taken together, these observations suggest an increase in bubble holdup due, perhaps, to an increase in the rate of coalescence at small a.c.d.'s.

The mean bubble radius was found to be strongly dependent on anode inclination, electrode rotation rate and current density. The evolution of smaller bubbles was favoured at high angles of inclination of the anode, high anode rotation rates, low cathode rotation rates and low current densities. Recently, Solheim *et al.* [20] showed that the melt velocity decreases with decreasing bubble size. Based on the present work the consequent decrease in mass transfer rate would be expected to result in an increase of current efficiency. Furthermore, the current efficiency measurements and resistance studies, under the conditions reported here, suggest the formation of a bubble layer thickness of ~ 1 cm, giving a practical limitation to the operational a.c.d.

Acknowledgements

We acknowledge the skilful assistance of Mr J. F. Kubacki, without whose efforts the design and construction of the electrochemical cell would not have been possible. We also thank Ms P. M. Hoobin and Ms C. McInnes for analytical services, and Mr P. Rummel and Mr J. McLeod for technical assistance. During the course of the work helpful discussions were held with Dr K. J. Cathro and Dr R. Woods of this laboratory, Dr M. P. Taylor and other research personnel of the Comalco Research Centre, Victoria, Australia. We further acknowledge the supply of melt and electrode materials from the Comalco Research Centre.

References

[1] R. C. Dorward, *J. Appl. Electrochem.* **13** (1983) 569.
[2] M. Karlsen, S. Rolseth and J. Thonstad, *Aluminium* **64** (1988) 615.
[3] D. Kasherman and M. Skyllas-Kazacos, *J. Appl. Electrochem.* **18** (1988) 863.
[4] *Idem, ibid.* **21** (1991) 716.
[5] W. D. Zhang, J. J. J. Chen, M. P. Taylor and B. J. Welch, *in* 'Chemeca 91', Vol. 2, Proc. 19th Australasian Chemical Engineering Conference, The Institution of Engineers, Australia (1991) pp. 721–7.
[6] T. Utigard and J. M. Toguri, *in* 'Light Metals 1985', The Metallurgical Society of AIME, Warrendale, USA (1985) pp. 405–13.
[7] K. J. Cathro, CSIRO, Division of Mineral Products, private communication (1992).
[8] R. P. Singh, J. H. Flint and D. R. Sadoway, *in* 'Energy Reduction Techniques in Metal Electrochemical Processes', (edited by R. G. Bautista and R. J. Wesely), The Metallurgical Society, Warrendale, USA (1985) pp. 155–62.
[9] K. Grjotheim, C. Krohn, M. Malinovsky, K. Matiasovsky and J. Thonstad, 'Aluminium Electrolysis', 2nd edn., Aluminium-Verlag, Düsseldorf (1982) pp. 130, 170.
[10] V. A. Ettel, B. V. Tilak and A. S. Gendron, *J. Electrochem. Soc.* **121** (1974) 867.
[11] J. W. Burgman and P. J. Sides, *Electrochim. Acta* **34** (1989) 841.
[12] K. Grjotheim, *et al., op. cit.* [9], pp. 326, 334–5.
[13] K. Grjotheim, *et al., op cit.* [9], Fig. 5.29, p. 155.
[14] J. A. Leistra and P. J. Sides, *Electrochim. Acta* **33** (1988) 1761.
[15] C. Gabrielli, F. Huet, M. Keddam and A. Sahar, *J. Appl. Electrochem.* **19** (1989) 683.
[16] T. M. Hyde and B. J. Welch, *in* 'The Eighth Australasian Electrochemistry Conference', February 1992, Royal Australian Chemical Institute & New Zealand Institute of Chemistry, Auckland, N.Z. (1992). Poster Paper PO 64.
[17] C. Gabrielli, F. Huet, M. Keddam, A. Macias and A. Sahar, *J. Appl. Electrochem.* **19** (1989) 617.
[18] E. W. Dewing, *Can. Met. Quart.* **30** (1991) 153.
[19] F. Lantelme, D. Damianacos and M. Chemla, *J. Electrochem. Soc.* **127** (1980) 498.
[20] A. Solheim, S. T. Johansen, S. Rolseth and J. Thonstad, *J. Appl. Electrochem.* **19** (1989) 703.